Quenching massive galaxies across cosmic time with the semi-analytic model SHARK v2.0 - Supplementary material

Claudia del P. Lagos[1,2,3]★, Matías Bravo[4], Rodrigo Tobar[1], Danail Obreschkow[1,2], Chris Power[1,2], Aaron S. G. Robotham[1,2], Katy L. Proctor[1,2], Samuel Hansen[1], Ángel Chandro-Gómez[1,2], Julian Carrivick[1]

[1]*International Centre for Radio Astronomy Research (ICRAR), M468, University of Western Australia, 35 Stirling Hwy, Crawley, WA 6009, Australia.*
[2]*ARC Centre of Excellence for All Sky Astrophysics in 3 Dimensions (ASTRO 3D).*
[3]*Cosmic Dawn Center (DAWN), Denmark.*
[4]*Department of Physics & Astronomy, McMaster University, 1280 Main Street W, Hamilton, ON, L8S 4M1, Canada.*

5 September 2023

ABSTRACT

In this supplementary material, we present additional comparisons between SHARK v1.1 (Lagos et al. 2018) and SHARK v2.0, and observations where possible. We demonstrate that the improvements of SHARK v2.0 over v1.1 discussed in length in the main paper have not come in the detriment of worsening the agreement with observations in areas in which SHARK v1.1 compared very favourably with observations, such as the galaxy luminosity function across wavelengths and cosmic time.

1 GAS MASS FUNCTIONS AND SCALING RELATIONS

In this section we show some key results that were originally presented in Lagos et al. (2018, hereafter L18).

Fig. 1 shows the atomic hydrogen (HI) and molecular hydrogen (H_2) mass function at $z = 0$ for SHARK v2.0 and L18 compared with observations. In general both models produce similar results at $M_{\rm HI} \lesssim 10^{10.75}\,{\rm M}_\odot$ and are in reasonable agreement with observations in that range. SHARK v2.0 predicts a slightly flatter low-mass end of the HI mass function (specially noticeable at HI masses in the range $10^{7.5} - 10^{9}\,{\rm M}_\odot$). The main difference is the higher number density of very massive HI galaxies, $M_{\rm HI} \gtrsim 10^{10.75}\,{\rm M}_\odot$, of which SHARK v2.0 predicts too many compared to observations and compared to SHARK v1.1. This is not necessarily surprising as this was not used as a constraint in OPTIM. In the future, we will investigate the joint constraint of the stellar and HI mass functions. For the H_2 mass function, SHARK v2.0 and v1.1 predictions are very similar in the range in which there are observational constraints. At H_2 masses $\gtrsim 10^{10.5}\,{\rm M}_\odot$, SHARK v2.0 predicts a higher number density than v1.1, but the difference is smaller than that seen for the HI mass function.

Fig. 2 shows the neutral (HI+H_2), HI and H_2 dependence on stellar mass for galaxies in SHARK v2.0 at $z = 0$ compared with observations. The gas scaling relations in SHARK v2.0 are in excellent agreement with observations of xGASS and xCOLDGASS, which are surveys designed to be selected by stellar mass and hence the fairest comparison with what we show for the model. It is only in the most massive two mass bins that we see SHARK v2.0 predicting a lower median than the observations. However, this is not a concern for the most massive bin in the HI and H_2-stellar mass scaling relations as the median is unconstrained there for the observations (> 50% of the galaxies were non-detections). Note that here we have not attempted to match the observations by stellar mass, mix of centrals and satellites and redshift distribution, as it has been done in other simulations and shown to have an effect in the level of agreement one can obtain with the observations (Stevens et al. 2019, 2021).

The contour levels of Fig. 2 reveal that galaxies in SHARK v2.0 start to display signs of quenching in the form of gas depletion, at stellar masses slightly below $10^{10}\,{\rm M}_\odot$, where a significant tail of gas fractions below 10^{-3} emerges.

2 THE ABUNDANCE OF MOLECULAR AND ATOMIC GAS ACROSS COSMIC TIME

Fig. 3 shows the evolution of the cosmic density of HI and H_2 in SHARK v2.0 and L18, compared with observations. Both models predict similar cosmic gas densities, with the biggest difference seen in the H_2 density in SHARK v2.0 peaking at $z \approx 2.5$ compared with a peak at $z \approx 1.5$ in L18.

Regarding the HI density, we see that both SHARK v2.0 and L18 agree with observations within the scatter at $z \lesssim 1.5$. At higher redshifts, the model clearly predicts too low HI densities. However, a big caveat here is that for both models we plot the total HI in galaxies, which is what the model naturally tracks, while observations trace the total HI content of the Universe. Cosmological hydrodynamical simulations indicate that at $z \gtrsim 1$, most of the HI is found not in galaxies but in the circumgalactic medium (CGM) (Diemer et al. 2019; Garratt-Smithson et al. 2021). We conservatively show a vertical line at $z = 2$ indicating that above that redshift most of the HI should be in the CGM rather than galaxies. The top panel of Fig. 3 shows observations at $z > 4$ from Heintz et al. (2022) attempting to infer the HI content in galaxies rather than the total in the early Universe. They do that by using a calibration of the [CII]-HI relation, which is metallicity-dependent, and applying it to [CII] detections obtained from the Atacama Large Millimeter Array (ALMA). This measurement has many potential systematic effects that are unaccounted for in the errorbars, but it is interesting to see that it indicates an order of magnitude less HI density associated to galaxies compared to the total. We show for reference the total neutral gas density associated to galaxies in SHARK v2.0 (red dotted line), to show that this obser-

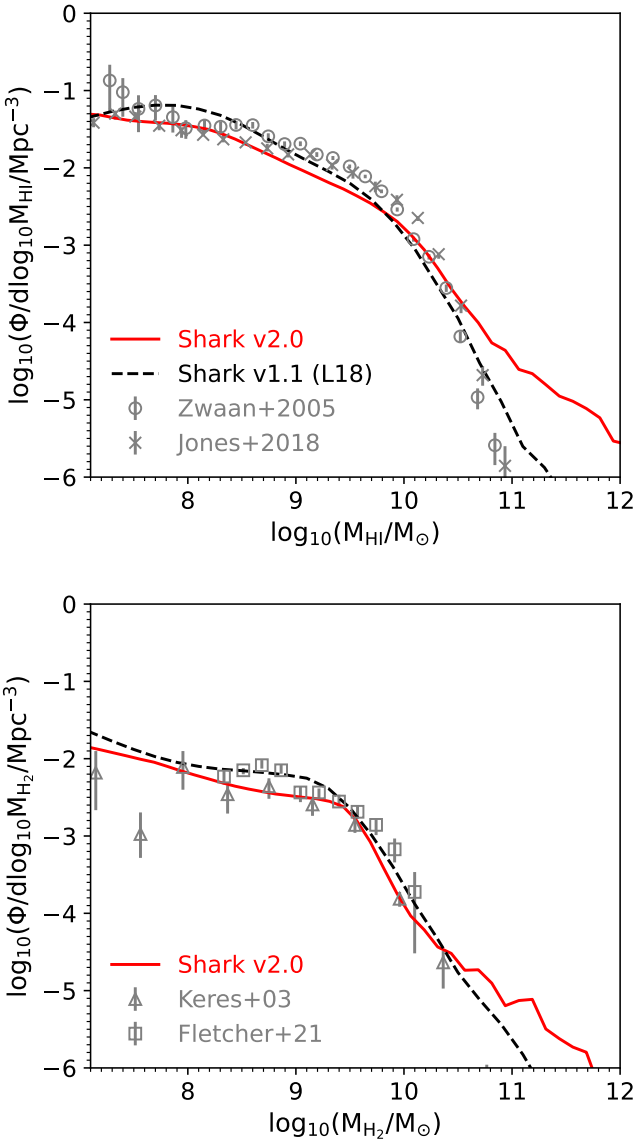

Figure 1. HI (top) and H_2 (bottom) mass function at $z = 0$ for Shark v2.0 (solid line) and L18 (dashed line). Observations from Zwaan et al. (2005); Jones et al. (2018); Keres et al. (2003); Fletcher et al. (2021) are shown as symbols, as labelled.

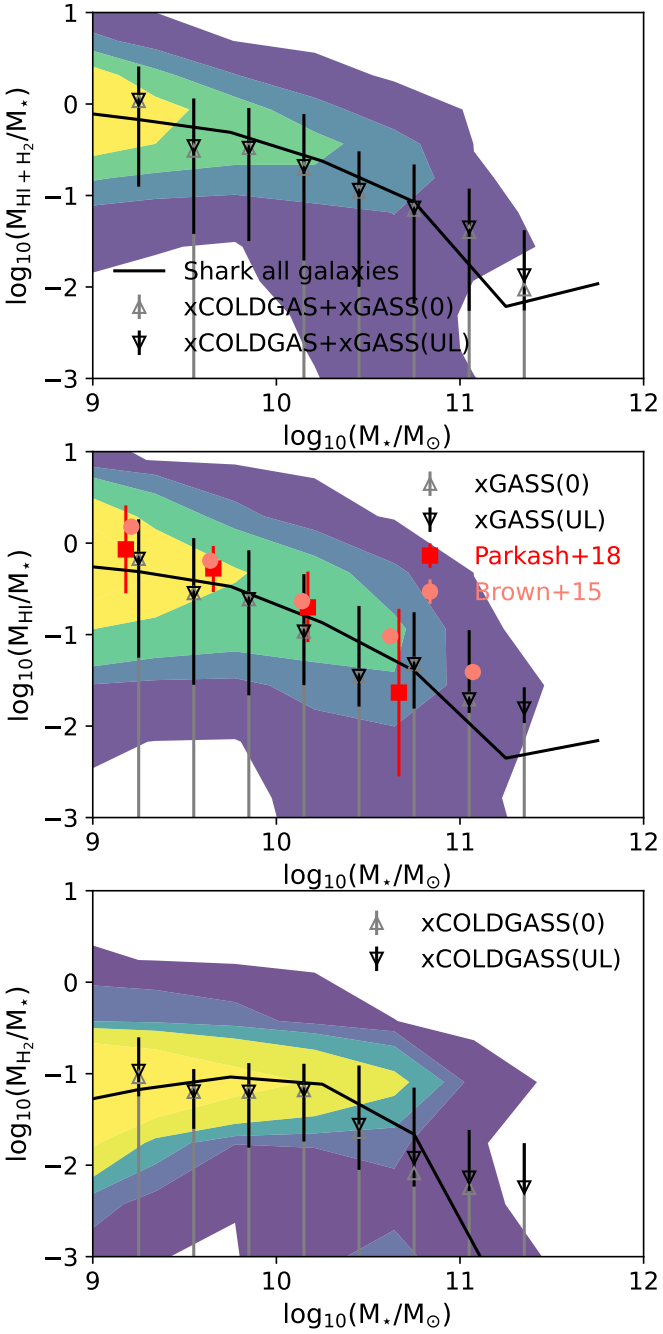

Figure 2. Gas-stellar mass scaling relations for: total neutral gas (top panel), HI (middle panel) and H_2 (bottom panel) at $z = 0$ for Shark v2.0. Medians are shown as black lines while the contours show percentile ranges from 99th to 10th. Observations from xGASS (Catinella et al. 2018), xCOLDGAS (Saintonge et al. 2017) and from Brown et al. (2015); Parkash et al. (2018), are shown as symbols. Downwards triangles show the xGASS/xCOLDGASS observations if non-detections are set to their upper limit, while upward triangles show the results of non-detections are set to zero. Similarly with errorbars associated to xGASS and xCOLDDGASS, we use black errorbars to show the 16th – 84th percentile ranges if non-detections are set to their upper limit, or gray errorbars if they are set to 0. Note that for the middle and bottom panels, the median from xGASS and xCOLDGASS in the highest stellar mass bin is unconstrained.

vational datapoint falls between our predicted cosmic HI and total neutral density (of gas in galaxies).

The lower panel of Fig. 3 focuses on H_2, and shows that within the uncertainties, both Shark v2.0 and L18 agree reasonably well with observations.

3 METALLICITY-STELLAR MASS RELATIONS IN THE LOCAL UNIVERSE

Fig. 4 shows the gas-phase and stellar metallicities as a function of stellar mass for galaxies at $z = 0$ in Shark v2.0. We show the entire galaxy population in red and the subsample of actively star-

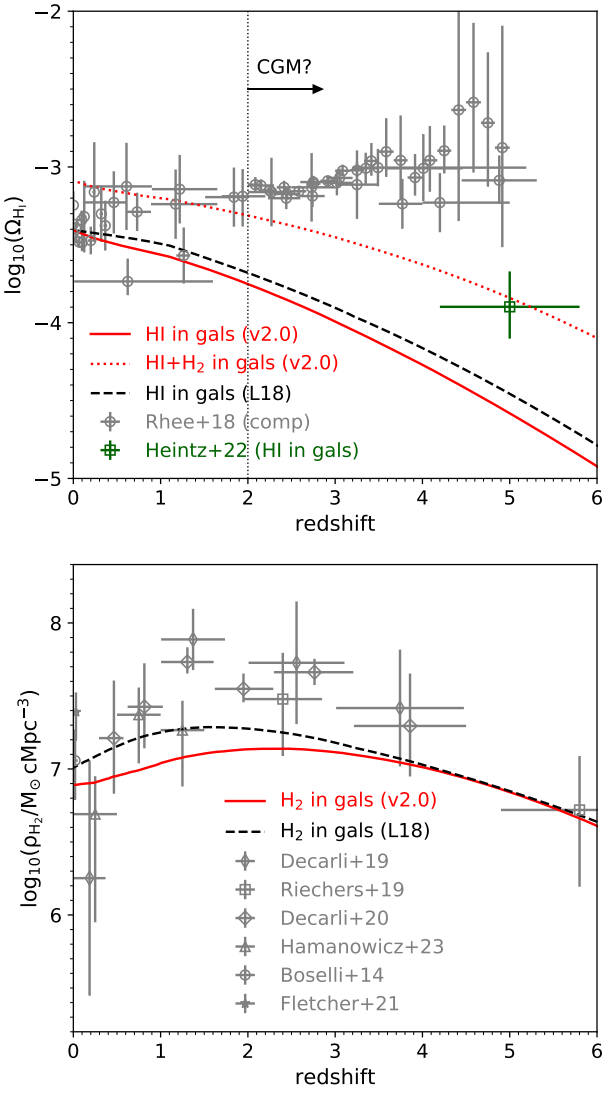

Figure 3. *Top panel:* Evolution of $\Omega_{\rm HI} \equiv \rho_{\rm HI}/\rho_{\rm crit}$, with $\rho_{\rm HI}$ and $\rho_{\rm crit}$ being the HI and critical densities, respectively. This is shown for SHARK v2.0 (solid line) and L18 (dashed line). We also show as dotted line the total neutral gas density (HI+H_2) for SHARK v2.0. Observations compiled by (Rhee et al. 2018) are shown as symbols. The latter are meant to represent the total HI in the Universe (within and outside galaxies). We also show observations from Heintz et al. (2022), which attempt to measure the HI density associated to galaxies. The vertical dotted line shows the regime in which HI is likely to mostly reside outside galaxies in the CGM. *Bottom panel:* As in the top panel but for the H_2 cosmic density, $\rho_{\rm H_2}$. Here we show observations from Boselli et al. (2014); Fletcher et al. (2021); Decarli et al. (2019, 2020); Riechers et al. (2019); Hamanowicz et al. (2023).

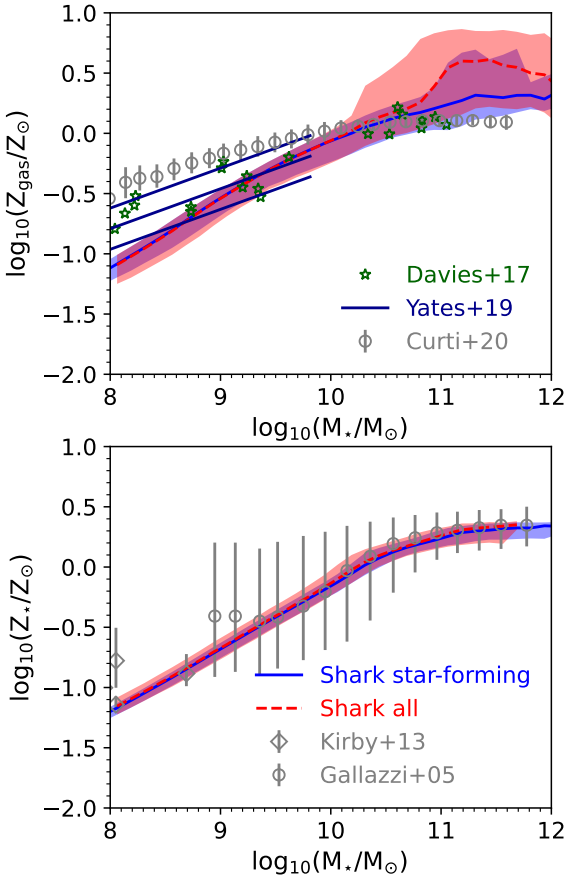

Figure 4. *Top panel:* Gas metallicity as a function of stellar mass for galaxies with a specific star formation rate $\geqslant 10^{-11}\,{\rm yr}^{-1}$ (considered star-forming; blue) and all galaxies (red) at $z = 0$ in SHARK v2.0. Lines with shaded regions show the median and $16^{\rm th}$ – $84^{\rm th}$ percentile ranges, respectively, for bins with $\geqslant 10$ galaxies. Observations of gas-phase metallicites derived via the direct electron temperature method from Yates et al. (2020); Curti et al. (2020) are shown, as labelled. We also show individual abundances derived in nearby galaxies from stellar spectroscopy of supergiant stars from Davies et al. (2017) as individual star symbols. To convert observed metallicities from $12 + \log_{10}({\rm O/H})$ to $\log_{10}(Z_{\rm gas}/Z_\odot)$ we subtract the solar metallicity ($12 + \log_{10}({\rm O/H})_\odot = 8.69$) to the former values. *Bottom panel:* As in the top panel but for stellar metallicity. We show observations from Gallazzi et al. (2005); Kirby et al. (2013), as labelled.

forming galaxies (i.e. those with a specific star formation rate, sSFR> $10^{-11}\,{\rm M}_\odot$) in blue.

The gas-phase metallicity-stellar mass relation in SHARK v2.0 appears to be slightly too steep at stellar masses $< 10^{10}\,{\rm M}_\odot$ compared to observations, but still within their scatter. Note that because most of the galaxies with $M_\star < 10^{10}\,{\rm M}_\odot$ are star-forming in SHARK, there is virtually no difference between the gas-phase metallicity-stellar mass relation of all galaxies and the subsample that is star-forming. If we compared the gas-phase metallicity-stellar mass relation of the entire galaxy population with observations at the massive end ($M_\star \gtrsim 10^{10.7}\,{\rm M}_\odot$, SHARK v2.0 appears to produce galaxies that are too metal rich. However, this is due to many of these massive galaxies being effectively passive and having very small masses of very chemically-enriched gas. If we select galaxies to be star-forming, which better resembles the type of galaxies observations use to derive the gas-phase metallicity-stellar mass relation, we see the flattening now behaving much more like the observations, with metallicities being at most 0.1 – 0.2 dex too large compared with observations. Such differences are well within the systematic uncertainties associated to measuring gas metallicities (Kewley & Ellison 2008).

The stellar metallicity-mass relation of SHARK v2.0 is in excellent agreement with observations, as shown in the bottom panel of Fig. 4. This level of agreement is similar to that shown in L18 for SHARK v1.1 (see their Fig. 15).

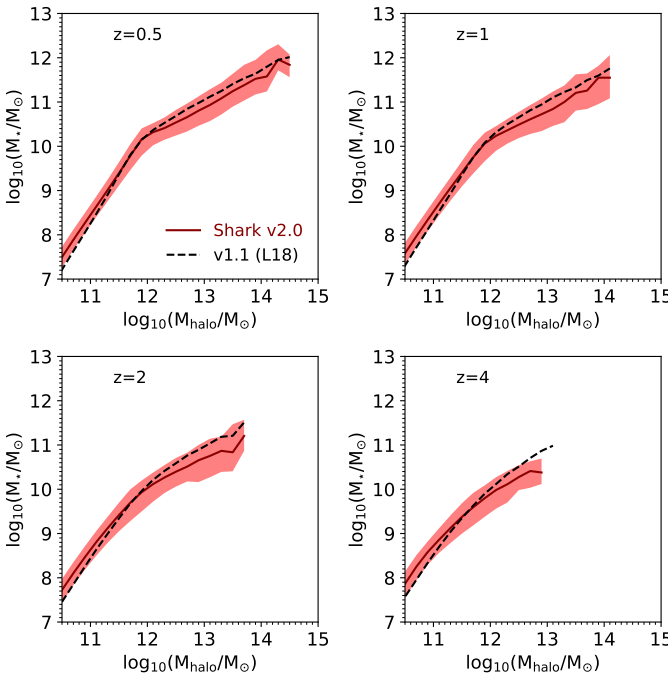

Figure 5. The stellar-halo mass relation for central galaxies in Shark v2.0 (red) and v1.1 (black; L18) from $z = 0.5$ up to $z = 4$, as labelled. Lines show medians for bins with $\geqslant 10$ galaxies, while the shaded regions show the $16 - 84^{\rm th}$ percentile ranges for Shark v2.0 only.

4 THE STELLAR-HALO MASS RELATION ACROSS COSMIC TIME

Fig. 5 shows the stellar-halo mass relation at different redshifts for central galaxies in Shark v2.0 and v1.1 (L18). Overall, there is a clearer break of the stellar-halo mass relation in Shark v2.0 compared with v1.1, which happens at around $M_{\rm halo} \gtrsim 10^{11.8}\,{\rm M}_{\odot}$. At all redshifts analysed here and at $M_{\rm halo} \gtrsim 10^{11.8}\,{\rm M}_{\odot}$, the stellar masses of Shark v2.0 centrals are smaller than in v1.1 by up to 0.5 dex. This is a direct consequence of the new AGN feedback model being able to quench massive galaxies more effectively at all cosmic times than the model adopted in L18. The opposite happens in halos with masses $M_{\rm halo} \lesssim 10^{11.8}\,{\rm M}_{\odot}$, where centrals in Shark v2.0 tend to be slightly more massive than in v1.1 by ≈ 0.3 dex. This is due to the stellar feedback parameters adopted in the default model presented with Shark v2.0 leading to a weaker stellar feedback than v1.1.

In Shark v2.0 we also see that the scatter in stellar mass at fixed halo mass tends to increase with increasing halo mass. This was not the case in v1.1 (see Fig. 7 in L18), where there was a weak trend of the scatter *decreasing* with increasing halo mass, at least at $M_{\rm halo} \gtrsim 10^{12.5}\,{\rm M}_{\odot}$. The increasing scatter seen in v2.0 is consistent with the overall larger scatter in sSFRs associated with massive galaxies and black holes, and the overall larger diversity of star formation histories of massive galaxies (see Figs. 9 and 10 of the main paper).

5 THE STAR FORMATION RATE FUNCTION ACROSS COSMIC TIME

Fig. 6 shows the star formation rate (SFR) function from $z = 0$ to $z = 8$ for Shark v2.0 and v1.1 (L18) compared with a compilation of observations coming from different SFR photometric proxies, from the ultraviolet to the radio continuum.

Overall, Shark v2.0 and v1.1 produce similar SFR functions up to $z = 3$. At higher redshifts, Shark v2.0 produces a higher number density of galaxies across the dynamic range of SFRs studied here by up to ≈ 0.3 dex compared with Shark v1.1. This is consistent with the overall higher CSFRD of Shark v2.0 at $z > 3$ compared to v1.1 shown in Fig. 3 of the main paper. Both versions of Shark are in good agreement with observations up to $z = 3$, and at higher redshifts v2.0 gives an overall better fit to the observations than the parameters adopted in L18.

6 GALAXY LUMINOSITY FUNCTIONS ACROSS COSMIC TIME

One of the key successes of Shark v1.1 is the level of agreement between the predicted galaxy luminosity functions (LFs) and observations presented in Lagos et al. (2019), and the fact that Shark v1.1 was able to simultaneously reproduce the optical and near-infrared (NIR) and sub-millimeter (sub-mm) emission of galaxies at different redshifts without the need of fine tuning. In this section we show that the level of agreement between Shark v2.0 and observations of the galaxy LF at different wavelengths and redshifts remains similar to what was reported in Lagos et al. (2019, 2020).

We compute galaxy SEDs using the preferred method introduced in Lagos et al. (2019), which is described in the bullet points below:

- We first compute the dust mass of galaxies following the empirical relation between gas metallicity and the dust-to-gas mass ratio of Rémy-Ruyer et al. (2014) (referred to as "RR14" in Lagos et al. 2019).
- We compute the surface density of dust in disks and bulges, separately, as described in Section 2.2 of Lagos et al. (2019).
- We use the dust surface density to choose the dust attenuation parameters following the radiative transfer analysis of EAGLE galaxies presented in Trayford et al. (2020).
- We then use Viperfish[1] to extract the Shark SFHs, metallicity histories (ZFH), and attenuation parameters to then input into ProSpect[2] to produce the galaxy spectrum and convolve it with a series of input broad-band filters. The latter produces the apparent and absolute magnitudes of the whole galaxy, as well as per galaxy component, separating disks, and bulges. For bulges, we also independently output the light coming stars in the bulge that were formed in-situ or transferred to the bulge via disk-instabilities or galaxy mergers.

The method above was referred to as "EAGLE-τ RR14" in Lagos et al. (2019).

Fig. 7 shows the GALEX FUV, NUV, and SDSS ugriz LFs at $z = 0$ for Shark v2.0. This figure shows the equivalent to Fig. 10 in Lagos et al. (2019), which was presented for Shark v1.1. For the bands GALEX FUV, NUV and SDSS u, we find that Shark v2.0 produces a slightly brighter end of the LF compared to v1.1 by 0.3 – 0.4 mag, worsening the agreement with observations. We find that this is largely driven by the greater contribution of light from bulges formed via disk instabilities. In Shark v1.1 they had a contribution similar to bulges built via galaxy mergers, while in v2.0 their contribution increased by an order of magnitude at the

[1] https://github.com/asgr/Viperfish/
[2] https://github.com/asgr/ProSpect

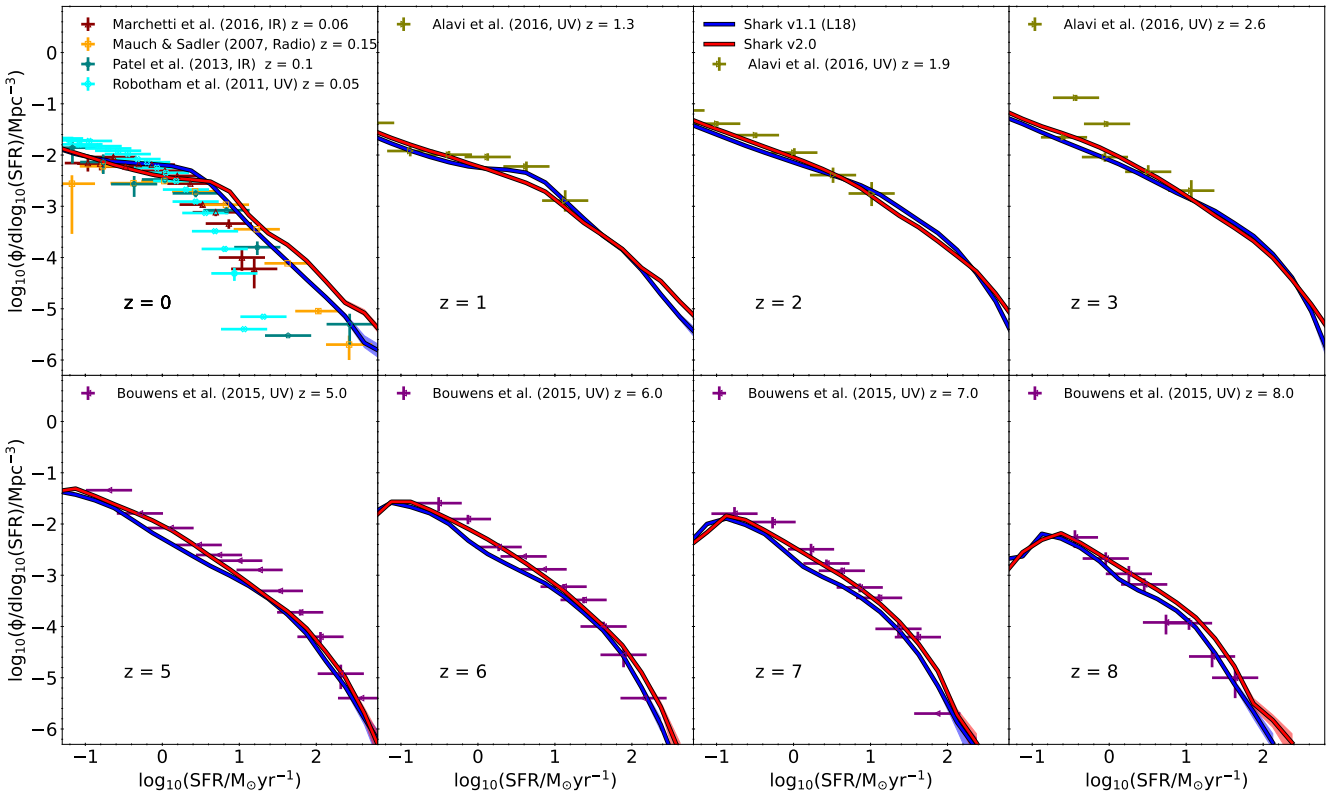

Figure 6. The SFR function from $z = 0$ to $z = 8$, as labelled, for SHARK v2.0 (red) and v1.1 (L18) (blue). Observations compiled by Katsianis et al. (2017) are also presented, as labelled. This compilation comprises data from Mauch & Sadler (2007); Robotham & Driver (2011); Patel et al. (2013); Bouwens et al. (2015); Marchetti et al. (2016); Alavi et al. (2016). Labels show the photometric proxy used to derive SFRs and the mean redshift of the sample in each of the papers shown.

bright end of the GALEX FUV LF, and 0.5 dex in the SDSS r-band. Those disk-instability-driven bulges correspond to recent starbursts in galaxies in SHARK v2.0.

In the SDSS g and r bands, SHARK v2.0 produces an end of the LF that is only 0.1 – 0.2 mag brighter than v1.1, and hence the agreement with observations continues to be satisfactory. The LFs for SDSS bands i and z in SHARK v2.0 are actually in better agreement with the observations than v1.1. This is especially clear below the break of the LF, where v1.1 was slightly underestimating the number density of faint galaxies, compared to an excellent agreement we see for SHARK v2.0.

Fig. 8 shows the $z = 0$ LFs for the VISTA YJHK bands, and IRAC 3.6μm, 4.5μm, 5.8μm and 8μm bands. This is the equivalent for SHARK v2.0 of Fig. 11 in Lagos et al. (2019), which was presented for SHARK v1.1. For the VISTA YJHK bands we find that SHARK v2.0 agrees better with observations than v1.1, again primarily thanks for the faint-end of the LFs producing a higher number density that better matches the observations. The contribution from bulges formed via disk instabilities in SHARK v2.0 is more significant than that what was seen in v1.1, in a way that they now dominate at the knee of the LF in all four VISTA bands, while in v1.1 they had a similar contribution to galaxy disks. For the IRAC bands, we overall see that SHARK v2.0 produces LFs that are very similar to those in v1.1. The main difference is again the increased contribution from bulges formed via disk instabilities, which is largely compensated in these bands by a decrease in the contribution of bulges built via mergers. The net result is thus a total LF that only slightly changed from the published work of Lagos et al. (2019).

Fig. 9 shows the $z = 0$ LFs in the far-infrared (FIR), at the Herschel PACS 160μm, SPIRE 250μm, 350μm and 500μm and the JCMT 850μm. This is the equivalent for SHARK v2.0 of Fig. 12 in Lagos et al. (2019), which was presented for SHARK v1.1. Overall, the FIR LFs predicted by SHARK v2.0 and v1.1 are very similar. The clearest change is again the higher contribution from bulges formed via disk instabilities. However, because in these bands and at $z = 0$, disk emission dominates at almost all magnitudes, we see little net difference in the total LF between the two versions of SHARK.

We now turn our attention to the evolution of the LFs. Fig. 10 shows the predicted rest-frame K-band LF from $z = 0.5$ to $z = 3$. The K-band LFs at $z = 0.5$, 1, 2 in SHARK v2.0 are very similar to those presented for v1.1 in Fig. 13 of Lagos et al. (2019) (the line of interest in that figure is the dotted purple line). At $z = 3$, we see SHARK v2.0 predicts a brighter end of the LF than v1.1 by ≈ 0.2 mag, and hence is in better agreement with the observations. Similarly to SHARK v1.1, we see in SHARK v2.0 that dust attenuation starts to become important even at the rest-frame K-band at $z = 3$ (see difference between thin and thick black lines), while at lower redshifts, dust attenuation is negligible at these wavelengths.

Fig. 11 shows the evolution of the FUV LF from $z = 3$ to $z = 10$. We find that SHARK v2.0 produces a much better agreement with the observations across all the redshifts shown than SHARK v1.1 when we compare to the same EAGLE-τ RR14 model (dotted purple line in Fig. 14 of Lagos19). Here, the impact of dust attenuation is important even at $z = 10$, which is especially acute at the bright-end of the FUV LF. Note that at $z = 3$, dust attenuation can reduce the FUV absolute magnitude of the brightest FUV galaxies by $\gtrsim 3$ mag. At $z = 10$, the

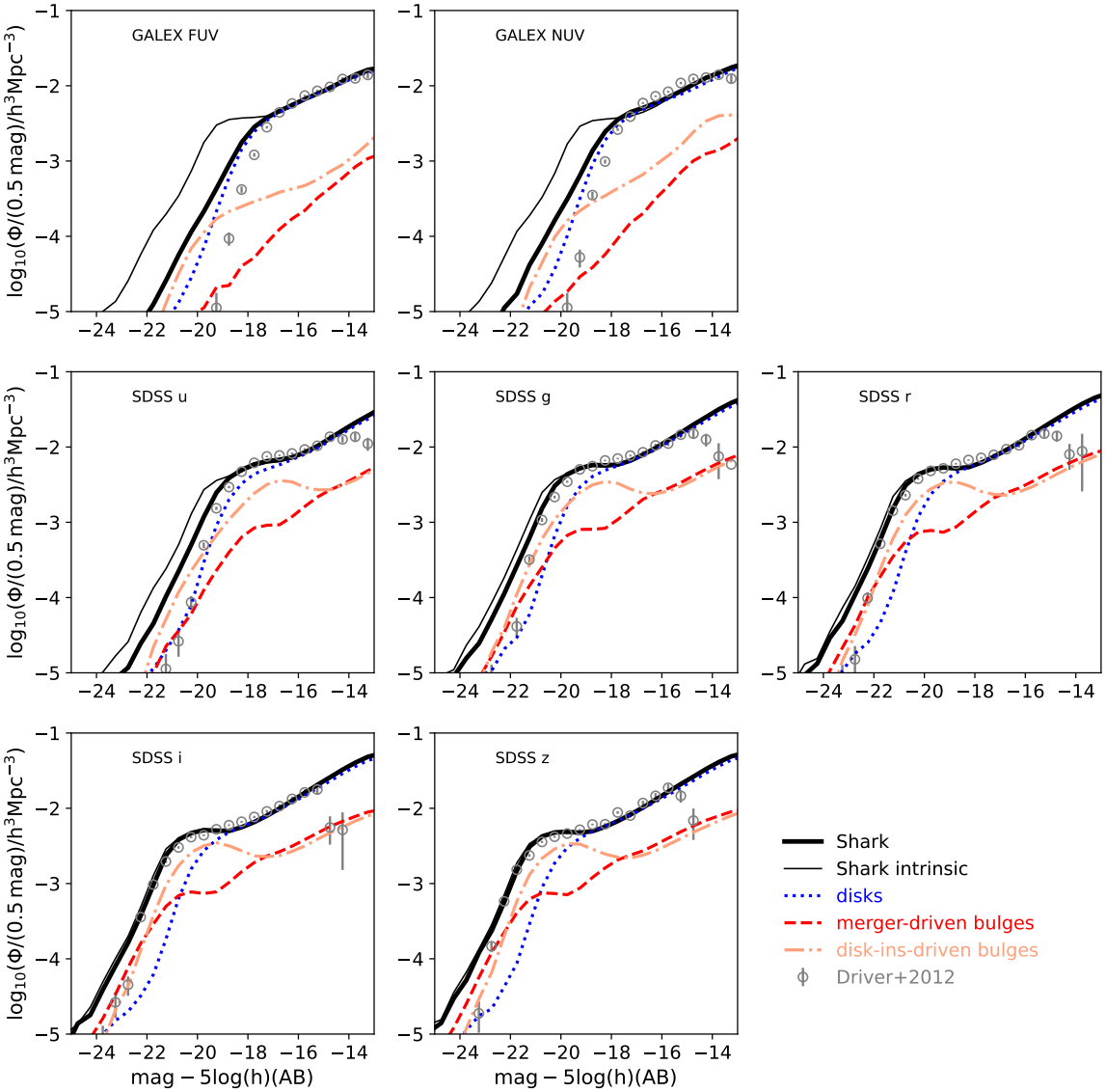

Figure 7. LFs at $z = 0$ of galaxies in Shark v2.0, for the GALEX FUV and NUV bands (top panels) and the SDSS u, r, g, i and z bands (middle and bottom panels), as labelled. We show as black thin and thick lines the emission before and after dust attenuation, respectively. The dotted, dashed and dot-dashed lines show contribution to the LF coming from disks, bulges that formed predominantly via galaxy mergers and by disk instabilities, respectively. The symbols show the observational measurements of Driver et al. (2012). Both the Shark v2.0 and observational luminosity functions are presented in bins of (0.5) mag, and thus the y-axis is not normalised by the adopted magnitude bin.

effect is smaller, but can still be as large as ≈ 2 mag in the intrinsically brightest FUV galaxies.

7 CONCLUSIONS

We have presented a range of additional comparisons between Shark v2.0, v1.1 (L18) and observations and convincingly show that areas in which v1.1 excelled (such as in the predictions of the panchromatic emission of galaxies across cosmic time), Shark v2.0 does similarly well. This reassures us that the improvements of Shark v2.0 over v1.1 discussed in length in the main paper have not come in the detriment of some of the key successes of Shark v1.1.

REFERENCES

Adams N. J., Bowler R. A. A., Jarvis M. J., Häußler B., McLure R. J., Bunker A., Dunlop J. S., Verma A., 2020, MNRAS, 494, 1771
Alavi A., Siana B., Richard J., Rafelski M., Jauzac M., Limousin M., Freeman W. R., Scarlata C. et al, 2016, ApJ, 832, 56
Boselli A., Cortese L., Boquien M., Boissier S., Catinella B., Gavazzi G., Lagos C., Saintonge A., 2014, A&A, 564, A67
Bouwens R. J., Illingworth G. D., Oesch P. A., Trenti M., Labbé I., Bradley L., Carollo M., van Dokkum P. G. et al, 2015, ApJ, 803, 34
Brown T., Catinella B., Cortese L., Kilborn V., Haynes M. P., Giovanelli R., 2015, MNRAS, 452, 2479
Catinella B., Saintonge A., Janowiecki S., Cortese L., Davé R., Lemonias J. J., Cooper A. P., Schiminovich D. et al, 2018, MNRAS, 476, 875
Cirasuolo M., McLure R. J., Dunlop J. S., Almaini O., Foucaud S., Simpson

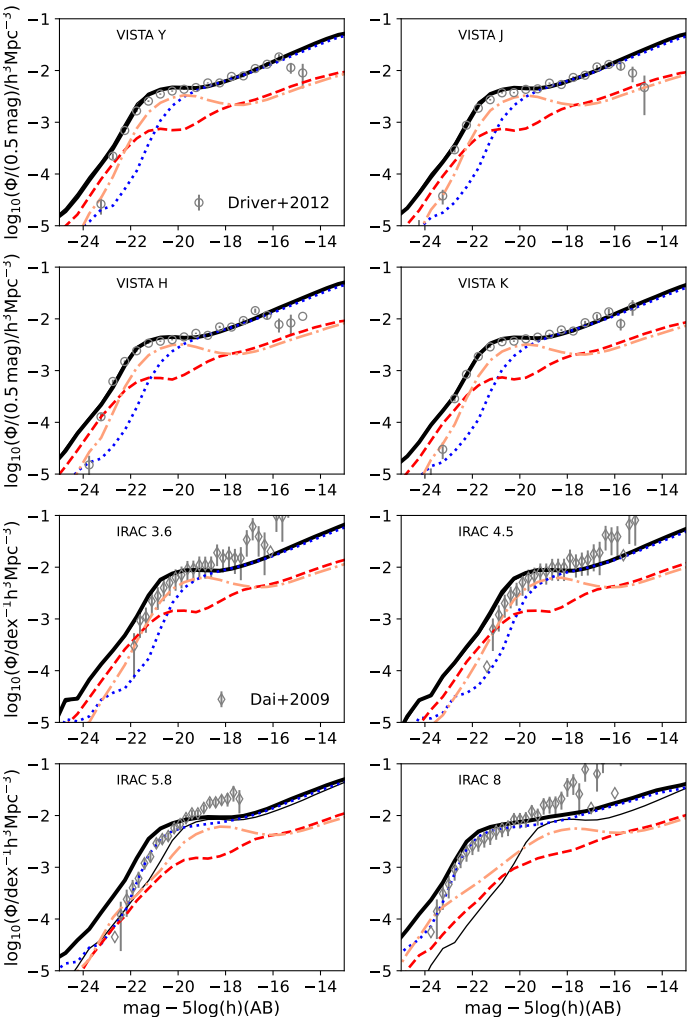

Figure 8. As in Fig. 7 but for the UKIDDS Y, J, H, K-bands, and IRAC 3.6μm, 4.5μm, 5.8μm and 8μm, as labelled in each panel. Symbols show the observational measurements of Driver et al. (2012) and Dai et al. (2009), as labelled. In the IRAC panels we show the number density normalised by the adopted x-axis bin, which is the way the LFs were presented in Dai et al. (2009).

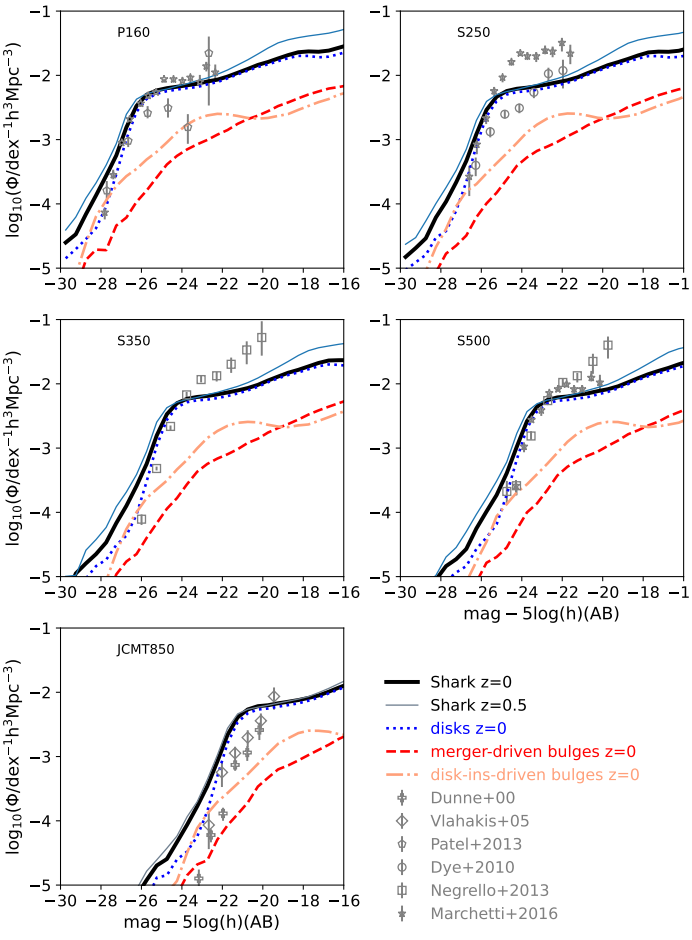

Figure 9. As in Fig. 7 for the Herschel PACS band 160μm, SPIRE bands 250μm, 350μm, 500μm and the JCMT 850μm, as labelled in each panel. We do not show intrinsic luminosities here, and instead the thin, solid line shows the $z = 0.5$ SHARK v2.0 LF prediction, as a reference to the level of evolution expected on that redshift window. This is useful to show as some of the observational estimates are computed with all the galaxies at $z \leqslant 0.5$. The symbols show the observational measurements of Dunne et al. (2000), Vlahakis et al. (2005), Dye et al. (2010), Patel et al. (2013), Negrello et al. (2013) and Marchetti et al. (2016), as labelled. Unlike Fig. 7, here the y-axis is normalised by the adopted x-axis bin.

C., 2010, MNRAS, 401, 1166
Curti M., Mannucci F., Cresci G., Maiolino R., 2020, MNRAS, 491, 944
Dai X., Assef R. J., Kochanek C. S., Brodwin M., Brown M. J. I., Caldwell N., Cool R. J., Dey A. et al, 2009, ApJ, 697, 506
Davies B., Kudritzki R.-P., Lardo C., Bergemann M., Beasor E., Plez B., Evans C., Bastian N. et al, 2017, ApJ, 847, 112
Decarli R., Aravena M., Boogaard L., Carilli C., González-López J., Walter F., Cortes P. C., Cox P. et al, 2020, ApJ, 902, 110
Decarli R., Walter F., Gónzalez-López J., Aravena M., Boogaard L., Carilli C., Cox P., Daddi E. et al, 2019, ApJ, 882, 138
Diemer B., Stevens A. R. H., Lagos C. d. P., Calette A. R., Tacchella S., Hernquist L., Marinacci F., Nelson D. et al, 2019, MNRAS, 487, 1529
Driver S. P., Robotham A. S. G., Kelvin L., Alpaslan M., Baldry I. K., Bamford S. P., Brough S., Brown M. et al, 2012, MNRAS, 427, 3244
Dunne L., Eales S., Edmunds M., Ivison R., Alexander P., Clements D. L., 2000, MNRAS, 315, 115
Dye S., Dunne L., Eales S., Smith D. J. B., Amblard A., Auld R., Baes M., Baldry I. K. et al, 2010, A&A, 518, L10
Finkelstein S. L., Ryan Jr. R. E., Papovich C., Dickinson M., Song M., Somerville R. S., Ferguson H. C., Salmon B. et al, 2015, ApJ, 810, 71
Fletcher T. J., Saintonge A., Soares P. S., Pontzen A., 2021, MNRAS, 501, 411
Gallazzi A., Charlot S., Brinchmann J., White S. D. M., Tremonti C. A., 2005, MNRAS, 362, 41
Garratt-Smithson L., Power C., Lagos C. d. P., Stevens A. R. H., Allison J. R., Sadler E. M., 2021, MNRAS, 501, 4396
Hamanowicz A., Zwaan M. A., Péroux C., Lagos C. d. P., Klitsch A., Ivison R. J., Biggs A. D., Szakacs R. et al, 2023, MNRAS, 519, 34
Heintz K. E., Oesch P. A., Aravena M., Bouwens R. J., Dayal P., Ferrara A., Fudamoto Y., Graziani L. et al, 2022, ApJ, 934, L27
Jones M. G., Haynes M. P., Giovanelli R., Moorman C., 2018, MNRAS, 477, 2
Katsianis A., Blanc G., Lagos C. P., Tejos N., Bower R. G., Alavi A., Gonzalez V., Theuns T. et al, 2017, MNRAS, 472, 919
Keres D., Yun M. S., Young J. S., 2003, ApJ, 582, 659
Kewley L. J., Ellison S. L., 2008, ApJ, 681, 1183
Kirby E. N., Cohen J. G., Guhathakurta P., Cheng L., Bullock J. S., Gallazzi

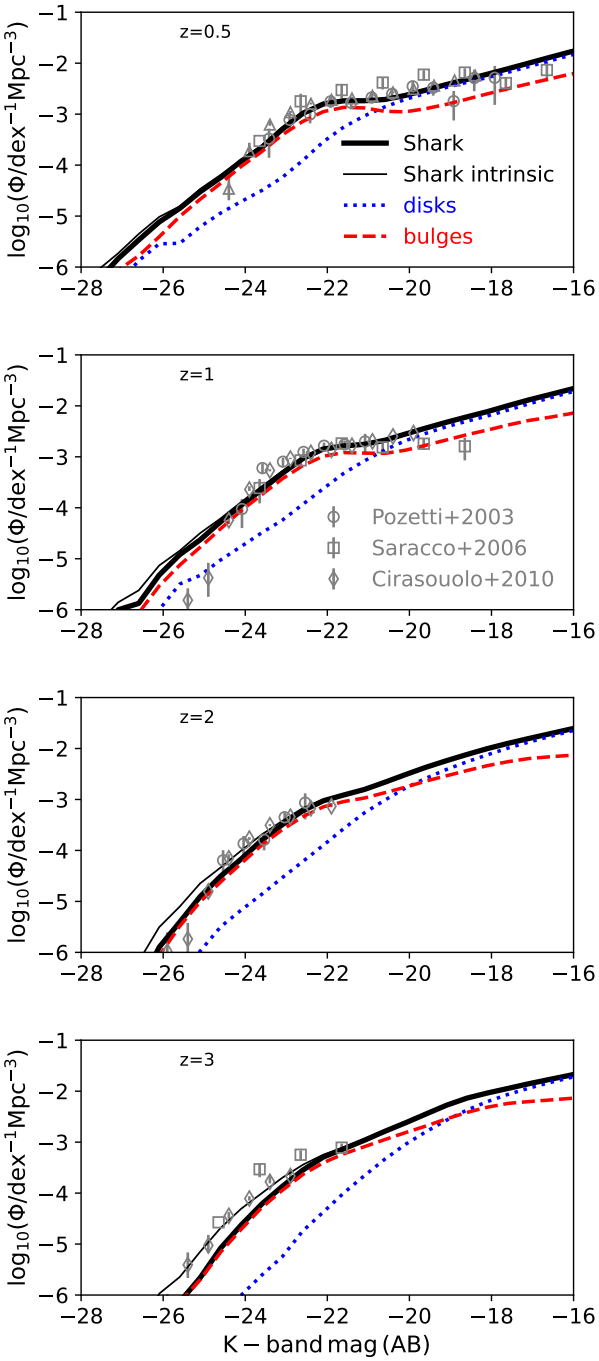

Figure 10. Rest-frame K-band LF from $z = 0.5$ to $z = 3$, as labelled, for Shark v2.0. The thin and thick black lines show the intrinsic and observed (i.e. after dust attenuation) emission, respectively. The contribution from disks and bulges are shown as blue and red lines, respectively. Note that here the contribution from bulges is the added one from bulges formed via disk instabilities and mergers. Observations from Pozzetti et al. (2003); Saracco et al. (2006); Cirasuolo et al. (2010) are shown as symbols, as labelled.

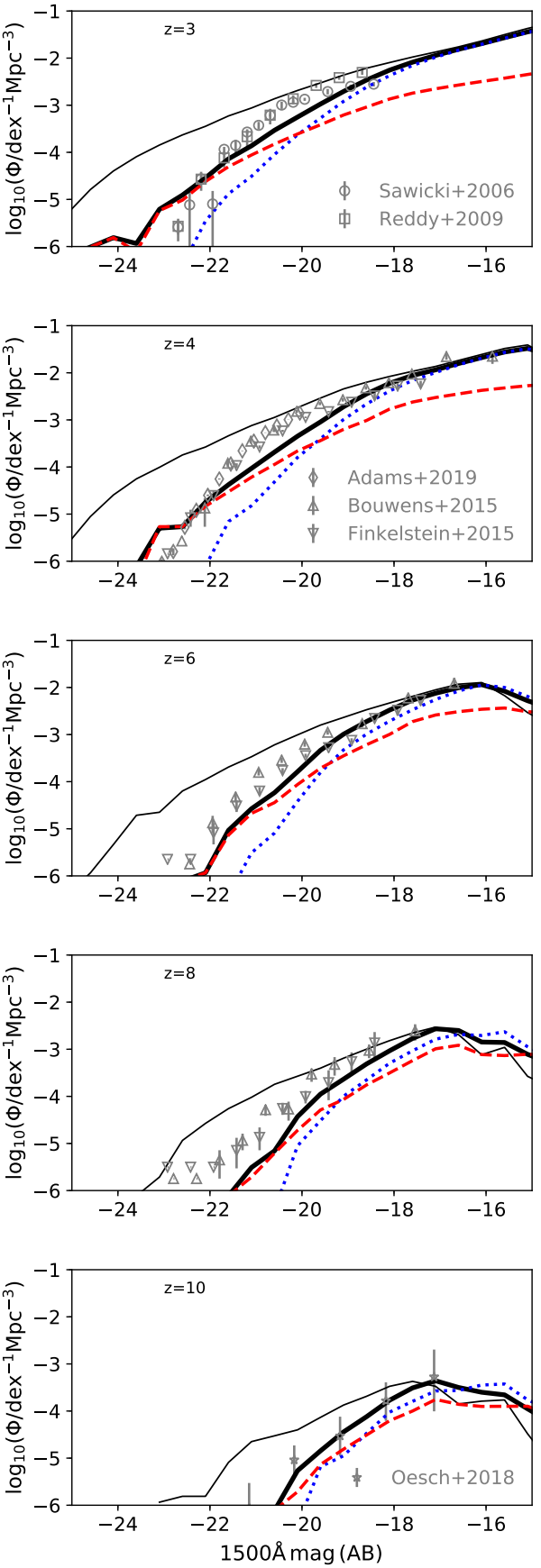

Figure 11. As in Fig. 10 but for the rest-frame FUV LF from $z = 3$ to $z = 10$, as labelled. Observations from Sawicki & Thompson (2006); Reddy & Steidel (2009); Bouwens et al. (2015); Finkelstein et al. (2015); Oesch et al. (2018); Adams et al. (2020) are shown as symbols, as labelled. Note that here, we calculate the absolute magnitude at 1500 using a top-hat filter around that wavelength.

A., 2013, ApJ, 779, 102
Lagos C. d. P., da Cunha E., Robotham A. S. G., Obreschkow D., Valentino F., Fujimoto S., Magdis G. E., Tobar R., 2020, MNRAS, 499, 1948
Lagos C. d. P., Robotham A. S. G., Trayford J. W., Tobar R., Bravo M., Bellstedt S., Davies L. J. M., Driver S. P. et al, 2019, MNRAS, 489, 4196
Lagos C. d. P., Tobar R. J., Robotham A. S. G., Obreschkow D., Mitchell

P. D., Power C., Elahi P. J., 2018, ArXiv:1807.11180
Marchetti L., Vaccari M., Franceschini A., Arumugam V., Aussel H., Béthermin M., Bock J., Boselli A. et al, 2016, MNRAS, 456, 1999
Mauch T., Sadler E. M., 2007, MNRAS, 375, 931
Negrello M., Clemens M., Gonzalez-Nuevo J., De Zotti G., Bonavera L., Cosco G., Guarese G., Boaretto L. et al, 2013, MNRAS, 429, 1309
Oesch P. A., Bouwens R. J., Illingworth G. D., Labbé I., Stefanon M., 2018, ApJ, 855, 105
Parkash V., Brown M. J. I., Jarrett T. H., Bonne N. J., 2018, ArXiv:1807.06246
Patel H., Clements D. L., Vaccari M., Mortlock D. J., Rowan-Robinson M., Pérez-Fournon I., Afonso-Luis A., 2013, MNRAS, 428, 291
Pozzetti L., Cimatti A., Zamorani G., Daddi E., Menci N., Fontana A., Renzini A., Mignoli M. et al, 2003, A&A, 402, 837
Reddy N. A., Steidel C. C., 2009, ApJ, 692, 778
Rémy-Ruyer A., Madden S. C., Galliano F., Galametz M., Takeuchi T. T., Asano R. S., Zhukovska S., Lebouteiller V. et al, 2014, A&A, 563, A31
Rhee J., Lah P., Briggs F. H., Chengalur J. N., Colless M., Willner S. P., Ashby M. L. N., Le Fèvre O., 2018, MNRAS, 473, 1879
Riechers D. A., Pavesi R., Sharon C. E., Hodge J. A., Decarli R., Walter F., Carilli C. L., Aravena M. et al, 2019, ApJ, 872, 7
Robotham A. S. G., Driver S. P., 2011, MNRAS, 413, 2570
Saintonge A., Catinella B., Tacconi L. J., Kauffmann G., Genzel R., Cortese L., Davé R., Fletcher T. J. et al, 2017, ApJS, 233, 22
Saracco P., Fiano A., Chincarini G., Vanzella E., Longhetti M., Cristiani S., Fontana A., Giallongo E. et al, 2006, MNRAS, 367, 349
Sawicki M., Thompson D., 2006, ApJ, 642, 653
Stevens A. R. H., Diemer B., Lagos C. d. P., Nelson D., Pillepich A., Brown T., Catinella B., Hernquist L. et al, 2019, MNRAS, 483, 5334
Stevens A. R. H., Lagos C. d. P., Cortese L., Catinella B., Diemer B., Nelson D., Pillepich A., Hernquist L. et al, 2021, MNRAS, 502, 3158
Trayford J. W., Lagos C. d. P., Robotham A. S. G., Obreschkow D., 2020, MNRAS, 491, 3937
Vlahakis C., Dunne L., Eales S., 2005, MNRAS, 364, 1253
Yates R. M., Schady P., Chen T. W., Schweyer T., Wiseman P., 2020, A&A, 634, A107
Zwaan M. A., Meyer M. J., Staveley-Smith L., Webster R. L., 2005, MNRAS, 359, L30

This paper has been typeset from a TEX/LATEX file prepared by the author.